

Initial Results of the MINDView PET Insert Inside the 3T mMR

Antonio J. Gonzalez^{1b}, Andrea Gonzalez-Montoro, Luis F. Vidal, Julio Barbera, Sebastian Aussenhofer, Liczandro Hernandez, Laura Moliner^{1b}, Filomeno Sanchez^{1b}, Carlos Correcher, Edwin J. Pincay, Gabriel Cañizares, Efthymios Lamprou, Sebastian Sanchez^{1b}, Juan V. Catret, Santiago Jiménez-Serrano, Jorge Cabello^{1b}, Markus Schwaiger, Amadeo Iborra^{1b}, Thibaut Merlin, Dimitris Visvikis^{1b}, and Jose M. Benlloch^{1b}

Abstract—Hybrid molecular and anatomical imaging devices, especially when simultaneously working, have shown to provide advantages over sequential acquisitions. In particular, we present in this preliminary study, the working performance of a brain positron emission tomography (PET) insert, within a 3T magnetic resonance imaging (MRI) system. To our knowledge, this is the largest PET system based on monolithic LYSO blocks. It consists of 60 scintillator blocks of 50 mm × 50 mm × 20 mm arranged in 3 rings of 20 detector modules each. An effective field of view (FOV) of 240 mm in diameter and 154 mm axially is defined. The crystals included a retroreflector layer at the entrance face, and are coupled to custom arrays of 12 × 12 silicon photomultipliers (SiPM), 3 mm × 3 mm each. Frontend electronics provide X and Y projections of the scintillation light by sampling each row and column of the SiPM arrays. The insert is thermally stabilized by using temperature-controlled air to about 27 °C. The PET insert has been installed at the Klinikum rechts der Isar (Munich) and tested within the whole-body Siemens biograph mMR, a 3T MRI combined with a PET scanner. A system sensitivity of almost 7% for an energy window of 350–650 keV was measured using a small size source at the center of the FOV (CFOV). Current system evaluation showed a spatial resolution at the CFOV of 1.7 mm using iterative algorithms, being below 2 mm within a centered diameter of 120 mm. Rods of a small Derenzo phantom of 2.5 mm were clearly resolved, independently of all tested

MRI sequences including echo-planar imaging, ultrashort time echo, MPrage, and T2-flair or arterial spin labeling. The PET insert did not show any count rate degradation also under those sequences for a variety of MR imaging acquisitions.

Index Terms—Brain positron emission tomography (PET), hybrid PET/MR insert, molecular imaging, monolithic crystals, silicon photomultipliers (SiPM).

I. INTRODUCTION

BRAIN positron emission tomography (PET) instrumentation has greatly evolved from its infancy, when it was used in regional localization, to currently providing excellent resolution with imaging characteristics that can notably impact clinical management [1]. Notice that the first PET scanner was already a dedicated brain PET system [2]. In brain imaging, as in most of other imaging modalities, combining functional, and anatomical information becomes very important, but also technologically challenging. This complementary information helps clinicians to for instance better localize the lesion under study. The predominant type of anatomical and functional imaging combination in brain has been PET and computed tomography. However, in the last decade there has been a significant push forward to develop simultaneous PET and magnetic resonance imaging (MRI) brain imaging. Whole-body PET-MRI systems have been used for brain studies [3], [4], among other applications.

With the aim of improving the image performance for brain studies, dedicated PET inserts have been developed in the past, as the one combined with the Siemens MAGNETOM Trio MRI [5], [6]. Another system was developed at Sogang University in Seoul, South Korea, using silicon photomultipliers (SiPMs) [7]. The system contains 72 detectors on a ring structure of 330 mm aperture using LYSO crystals of $3 \times 3 \times 20$ mm³. The SiPM signals are transmitted to preamplifiers using a 300 cm flexible flat cable. Also using SiPMs, a brain PET insert was developed at the National Institute of Radiological Sciences in Japan. A particular characteristic of this design is the use of four-layer DOI detectors integrated with the head coil of the MRI [8]. LGSO scintillators are arranged in $12 \times 4 \times 4$ layers. The size of each crystal element was 2.9 mm × 2.9 mm × 5.0 mm. It makes use of DOI

Manuscript received April 25, 2018; revised June 24, 2018; accepted August 13, 2018. Date of publication August 23, 2018; date of current version May 2, 2019. This work was supported in part by the European Union through FP7 Program under Grant 603002, in part by the European Research Council under the European Union's Horizon 2020 Research and Innovation Program under Grant 695536, in part by the Spanish Ministerio de Economía, Industria y Competitividad under Grant TEC2016-79884-C2-1-R, and in part by Ministerio de Economía y Competitividad through PROSPET under Grant DTS15/00152. (Corresponding author: Antonio J. Gonzalez.)

A. J. Gonzalez, A. Gonzalez-Montoro, L. F. Vidal, L. Hernandez, L. Moliner, F. Sanchez, E. J. Pincay, G. Cañizares, E. Lamprou, S. Sanchez, and J. M. Benlloch are with the Instituto de Instrumentación para Imagen Molecular, Centro Mixto CSIC—Universitat Politècnica de València, 46022 Valencia, Spain (e-mail: agonzalez@i3m.up.ves).

J. Barbera, J. V. Catret, and S. Jiménez-Serrano are with Oncovision, 46022 Valencia, Spain.

S. Aussenhofer is with NORAS MRI Products GmbH, 97204 Höchberg, Germany.

C. Correcher is with Bruker NMI, 46013 Valencia, Spain.

J. Cabello and M. Schwaiger are with Nuklearmedizin, Klinikum rechts der Isar, Technische Universität München, 81675 Munich, Germany.

A. Iborra, T. Merlin, and D. Visvikis are with LaTIM, INSERM, 29609 Brest, France.

Color versions of one or more of the figures in this paper are available online at <http://ieeexplore.ieee.org>.

Digital Object Identifier 10.1109/TRPMS.2018.2866899

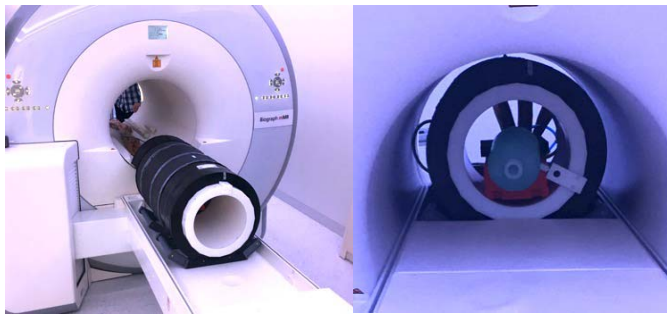


Fig. 1. Photographs of the MINDView PET insert. Left: it is shown when outside the MR ready to allocate patient head. Right: inserted in the MR while imaging a bottle.

information based on multilayer crystal arrays [9]. The detector and some electric components are packaged in a copper shielding box.

More recently, two projects were EU granted to build brain PET dedicated inserts. Both projects aim at developing instrumentation tools to clinically diagnose schizophrenia or depression, two major mental disorders. MRI and fMRI have shown to differentiate diagnosed schizophrenia from healthy controls only on a statistical basis. The utility of PET imaging here is practically limited by: the significant high cost, and the limited sensitivity and resolution of current scanners. The TRIMAGE research project develops an integrated brain PET-MRI-electroencephalogram scanner. The MRI has a compact 1.5-T cryogen-free magnet and the PET scanner is based on SiPM technology [10]. Two LYSO crystal arrays layers with 8 and 12 mm height and 3.3 mm pixel size will be mounted. The inner PET diameter is 312 mm with an axial length of 167 mm. The second project refers to the MINDView project [11]. We report in this paper the current status performance of the brain PET insert developed under the MINDView project, see photographs in Fig. 1.

This paper does not intend to exhaustively follow the NEMA standard but to demonstrate the working performance of the designed and constructed brain PET insert. It has been recently installed at the nuclear medicine department in Klinikum rechts der Isar (Munich) and also exhaustively tested inside the Siemens mMR, a whole body PET-MR with a 3T main magnetic field. A variety of MR sequences routinely used for brain imaging (including those for PET attenuation correction) have been run, and the PET response measured.

II. MATERIALS AND METHODS

A. Detector Blocks

The MINDView PET insert is composed by three rings of 20 detector blocks each [11], [12]. The detector blocks include a thick monolithic LYSO crystal with dimensions of 50 mm × 50 mm × 20 mm. The crystals have all faces polished, with their laterals black painted and the entrance one coupled to a retroreflector layer. Accurate studies have shown the advantage of using a retroreflector layer at the entrance face of the monolithic crystal [13].

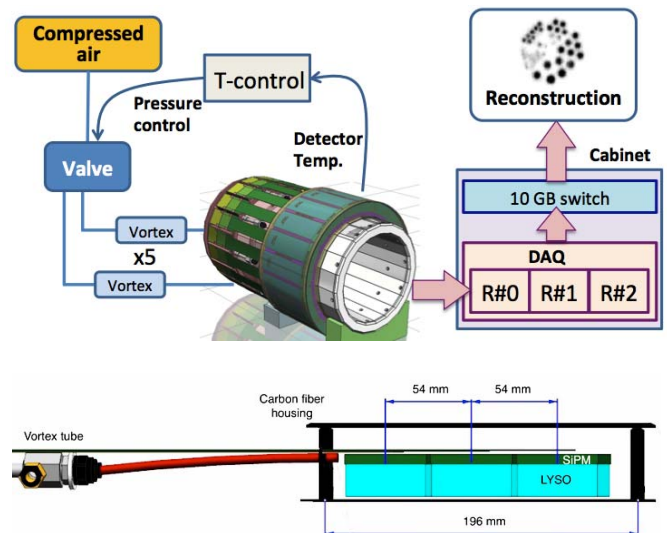


Fig. 2. Top: sketch of the system architecture: left blocks show the temperature control and right panels show the DAQ scheme. Bottom: lateral view example of the crystals position, SiPMs, carbon fiber housing, and vortex tube.

Each crystal is coupled to a custom array of 12×12 SensL SiPM (3 mm × 3 mm) with 4.36 mm pitch. SiPMs are of the MINDView-series type (similar to J-series) and were biased to about 30 V. The photosensor array is connected to an analog read-out electronics providing information for each row and column of such array. This read-out allows one to characterize the projected (X and Y) scintillation light distribution. Photon DOI is estimated from these projections as the average (X and Y) of the ratios of the energy to the maximum read-out signal (E/I_{\max}) [13]. Therefore, it is possible to determine the 3-D interaction position.

A trigger signal for each detector is conformed by summing all row signals. Typical rise and decay times for this signal are 25–50 ns and 200–300 ns, respectively. Each detector block includes a temperature sensor. All analog signals, as well as the temperature reading, are brought outside the MR field of view (FOV) using thin printed circuit boards that minimize nickel components and, thus, avoid MR distortions. They are fed into a data acquisition (DAQ) system using multicoaxial cabling.

The DAQ is formed by three sets of 10 ADC boards with 12 bits precision. Every ADC manages two detector blocks and are programmed with 250 ns charge integration windows. Each set of ten ADCs includes a trigger card, to which all 60 trigger signals from the detectors are fed. In this design, each trigger card controls the ADCs belonging to one PET ring (see sketch in Fig. 2). In practice the modular system behaves like three independent interconnected acquisition systems assembled in separated racks but all 60 detectors work independently. Time alignment between all ADCs (60 detectors) has been achieved taken special care in the design of the acquisition system in order to achieve a maximum intrinsic error of about 200 ps. Current coincidence window is 5 ns. Every detector has allowed coincidences with its nine opposite blocks in all rings.

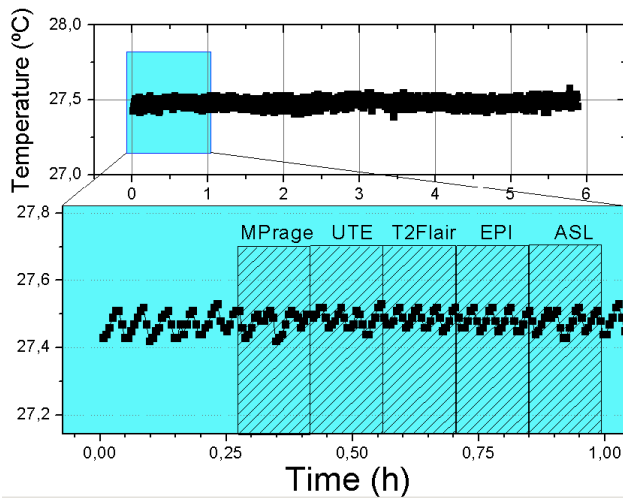


Fig. 3. Average system temperature for 7 h (nonstop) with different brain MR imaging sequences (top) and detail of the temperature when running specific MR sequences (bottom).

B. System Architecture

The distance from opposite crystal-to-crystal is about 330 mm. This, together with the allowed map of coincidences, defines a system FOV of 240 mm in diameter (transaxial) and 154 mm in the axial direction. The total volume of LYSO material is 3000 cm³, and the number of digitized signals as high as 1440 (total insert PET weight about 45 kg). These compare to about 9175 cm³ of LYSO and 4032 channels, for the PET within the Siemens mMR. The total scanner diameter including radio-frequency (RF) shielding is 42 cm, with an axial length of roughly 80 cm.

The whole DAQ electronics, together with detector blocks power supplies, and temperature regulation, are located in a cabinet that is nonferromagnetic and RF shielded.

The detector blocks are temperature stabilized using temperature controlled air flow, resulting after controlling the input pressure to five vortex tubes. The temperature sensors at the read-out electronics (near the SiPM arrays) are read and a PID controller manages the output air temperature, see Fig. 2. All PET measurements inside the MR were carried out at a stable average temperature (60 blocks) of 27.5 °C. As it can be seen in Fig. 3, the temperature spread during 7 h while continuously running MR sequences, was below 0.05 °C (sigma). A detail of one set of various sequences is also shown in Fig. 3. The temperature regulation is visible, however, even when running aggressive-pulsing sequences, such as ultrashort time echo (UTE) or echo-planar imaging (EPI), no effect on the average temperature was observed. This target temperature is a compromise between PET system performance and demanding air flow.

C. RF Coil and B0-B1 Fields Shielding

A dedicated RF coil with a birdcage configuration, transmit-receive, has been developed and simultaneously tested with the PET insert. It is made out of 16 rungs providing a geometric aperture of 25 cm, suitable for an ample and comfortable head allocation. The Siemens mMR has a 60 cm bore and an

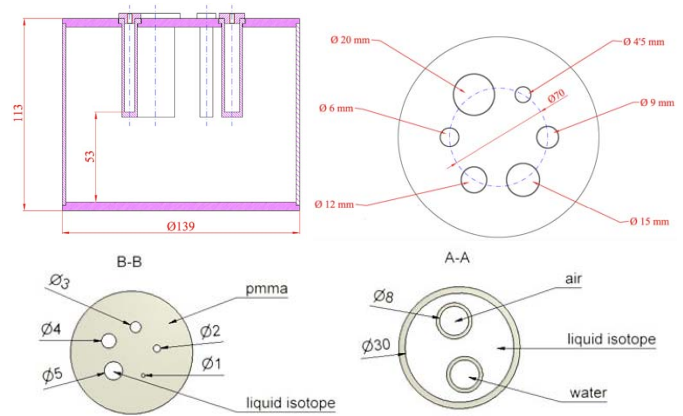


Fig. 4. Drawings of the phantoms used during the PET insert evaluation. Top row shows the recovery coefficients phantom filled with warm uniform background and six inserts. Next row shows the NEMA quality imaging phantom for small animals.

actively shielded whole-body gradient coil system (amplitude of 45 mT/m and slew rate of 200 T/m/s) [14]. The main MR sequences programmed to test the insert PET/MR compatibility have been EPI, arterial spin labeling, T1w (magnetization-prepared rapid gradient echo—MPPrage), T2w (fluid-attenuated inversion recovery—Flair), and UTE, which are regularly used in clinical routine for a variety of neuro-applications with the mMR scanner. Preventing electronic noise from the B1 field and possible eddy currents arising from the switching gradient field, have been achieved by implementing a Faraday-cage made out of 200 μ m overlaying carbon fiber sheets [15], see sketch in Fig. 2.

D. Sources and Phantoms

PET performance tests have been carried out using several encapsulated ²²Na sources as well as a variety of fillable phantoms namely a custom phantom with inserts in a warm background, NEMA imaging quality for small animals and a mini-Derenzo. The sources (1 inch \times 6 mm PMMA encapsulation) were 1 mm and 0.25 mm in diameter ²²Na sources with currently about 740 and 37 kBq activity, respectively.

A custom phantom was used to study the recovery coefficients in a large phantom. It has dimensions of 113 mm height and 139 mm in diameter in a warm background, and it includes six rods inserts with diameter ranging from 4.5 to 20 mm (height 55 mm), see Fig. 4. Several concentration ratios were tested, as it will be described below.

The small animal NEMA phantom is composed of a main fillable uniform region chamber, a lid that attaches to the main fillable region, containing two smaller cold region chambers, one that was filled with water and the other with air, and a solid acrylic glass region with five fillable rods drilled through with diameters of 1, 2, 3, 4, and 5 mm, respectively. The image-quality phantom was filled with ¹⁸F-FDG solution (32 MBq) and acquired applying a 350 to 650 keV energy window. Each acquisition lasted 180 s.

In the mini-Derenzo the rods diameters range from 1.5 to 6.5 mm in steps of 1 mm, with a pitch distance equals this diameter.

TABLE I
TESTS AND ALGORITHMS

Test	Algorithm	Voxel/Pixel	It./subs.
Spatial resolution	LMOS	0.7/1.4 mm	1 it/15 subs.
Spatial resolution	FBP	0.25-1 mm	
Recovery coeff.	MLEM	1/1 mm	10-24 it
IQ NEMA spatial res.	LMOS	1/2 mm	1 it/15 subs.
IQ NEMA MRI seq.	CASTOR	1/1 mm	2 it/10 subs.
Brain phantom	MLEM	1/1 mm	60 it

E. Reconstruction Methods

Regarding image reconstruction, we have used iterative algorithms, such as list mode ordered subsets (LMOS) [16], maximum likelihood expectation maximization (MLEM), as well as its accelerated variant ordered subsets MLEM (OSEM). The so-called IRIS projector is currently under investigation [17]. The purpose of using such variety of algorithms is to show there is not a bias of the scanner regarding the reconstruction method, and to also study if there is one that optimizes the results.

LMOS implements the tube of response projector and multiple CPU processing, and only scatter corrections are programmed during the reconstruction process. MLEM makes use of multiple graphical processing units (GPUs) capabilities and both scatter and random corrections considered. Virtual detector pixels between 1.4–2 mm have been tested, combined with voxel sizes of 0.7–1 mm. The open-source CASTOR platform [18] has been used to perform OSEM reconstructions, considering both virtual detector pixels and voxel sizes of 1 mm. The Siddon projector and OpenMP parallelism have been used for OSEM reconstructions. No scatter or random corrections are considered when using this method. Table I shows the algorithm method used for the different experiments, including number of iterations and/or subsets.

F. Detector Calibration

Every PET detector was position and energy calibrated using an already described procedure based on position-known sources [13], [19]. Notice that the 60 detectors were calibrated using an ^{18}F filled phantom with hot spots following an array distribution matching the holes of the Tungsten mask described in [13], covering an area of $46\text{ mm} \times 46\text{ mm}$. We collected around 10^7 coincidences for each detector block.

III. RESULTS

A. Detector Blocks Performance

The performance of the detector blocks used in this paper has been extensively reviewed in a prior publication [13]. Since there exist slight differences from that experimental first set-up to the finally constructed system, we show in Fig. 5 left flood maps of FDG sources (11×11 , 4.6 mm pitch) for three example detectors namely M19, M24, and M56 (corresponding each one to a different ring of detectors), as a function of the four DOI layers (5 mm thickness each). The first column shows the maps for the entrance layer, where stronger image compression is observed, as expected. The panel on the right

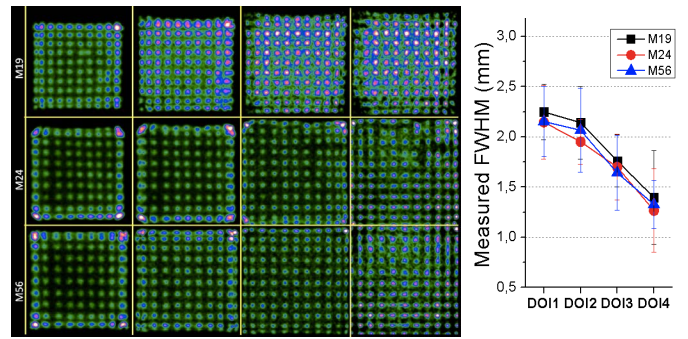


Fig. 5. Left: Flood maps for three detectors, one for each ring (top row M19, center row M26, and bottom row M56), of 11×11 collimated FDG sources, as a function of the DOI layer. From left to right, entrance crystal layer 20–15 mm (DOI1) to exit layer (closer to photosensor, DOI4) 5–0 mm. Right: measured spatial resolution (FWHM) versus DOI layer for these detectors.

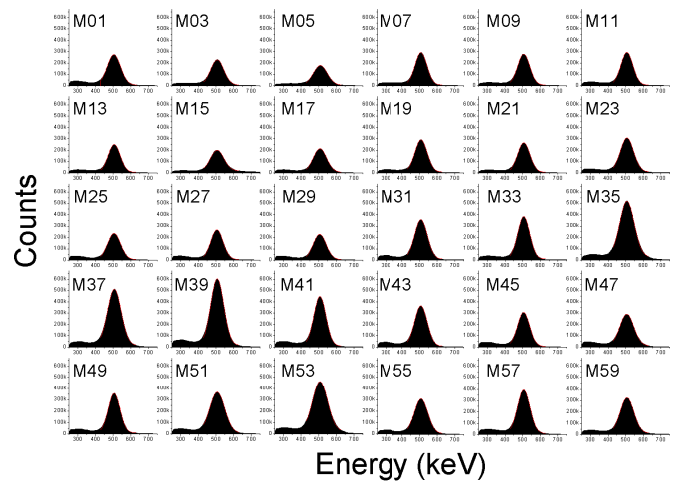


Fig. 6. Energy spectra for detectors with odd numbering.

hand side shows the measured FWHM for three detectors, also as a function of the DOI layer. By using a method based on software collimation [20], we have estimated the average intrinsic detector resolution for each detector block to be about 1.3 ± 0.1 mm.

We have determined the energy resolution of all detectors using one of the FDG fillable phantoms at the CFOV. Fig. 6 shows the energy spectra of detectors with odd module numbering. The spectra show all events happening in the crystal volume covered by the area of $46\text{ mm} \times 46\text{ mm}$. We measured an average energy resolution of $17.5\% \pm 1.5\%$ (standard deviation) for the entire system. The results shown in this paper do not include events in the last 2 mm region near the crystal edge.

The DOI was only analyzed using normal incidence collimated gamma ray beams [13]. We plot in Fig. 7 top-right and bottom panels, the DOI distributions, after calibration to millimeters, interactions contained in regions of interest defined at the center (M), lateral (L), and corners (C) of detector modules M01, M21, and M41. As an illustration, Fig. 7 top-left also shows the DOI distribution of detector M01 before calibration, where the different light scintillation truncations are

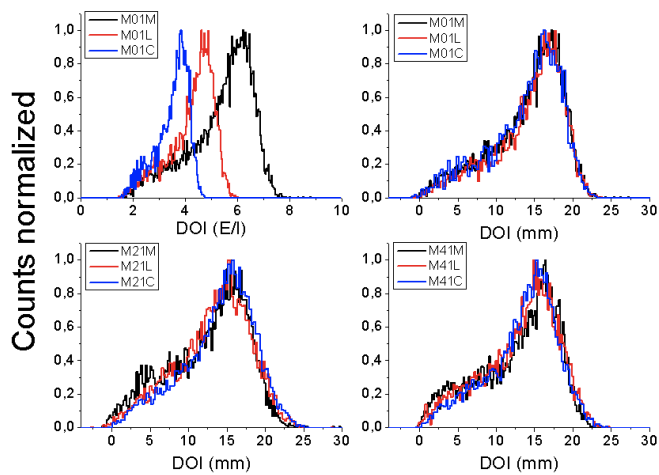


Fig. 7. Top-left: distributions before calibration for M01. Calibrated DOI distributions at the center (M), lateral (L), and corner (C), for modules M01, M21, and M41, are shown on top-right and bottom panels.

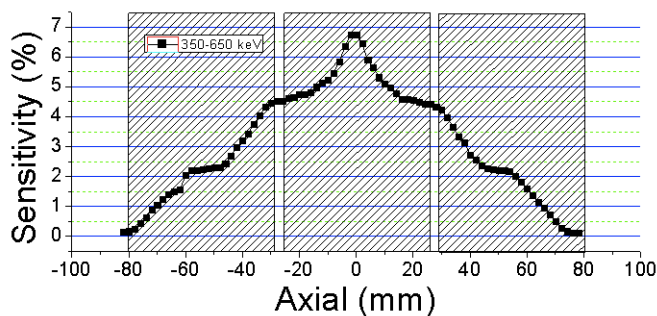


Fig. 8. Sensitivity plot measured with a small size ^{22}Na source across the axial FOV.

observed as a reduction of the upper limit of E/I. We expect DOI resolutions in the range of 4 ± 1 mm for all detectors.

B. PET Performance

The 1 mm ^{22}Na source was moved across the axial FOV, in steps of 0.5 mm, in order to measure the system sensitivity. Fig. 8 shows the measured sensitivity curve for an energy range of 350–650 keV. We observed almost 7% sensitivity at the CFOV, agreeing well with previous measurements with one ring [15] and also with expected values [12]. Noise equivalent count curves have not yet been analyzed but initial results show system capabilities to manage above 150 MBq within the FOV, without apparent image deterioration.

The 0.25 mm in diameter ^{22}Na source was moved along the radial axis, at three axial positions namely the center of the FOV, 1/4 and 3/8 of this axis. The data were reconstructed using LMOS with 0.7 mm voxels (cubic dimensions) and 1.4 mm virtual size pixels. One iteration and 15 subsets were selected [21]. As depicted in Fig. 9, the FWHM of the radial, transversal, and axial components at the CFOV are about 1.7 mm, degrading to 3 mm in the case of the radial and axial components, and to 2.2 mm in the case of the transversal at 100 mm off-radial distance. No significant deterioration is observed at other axial positions. The results show

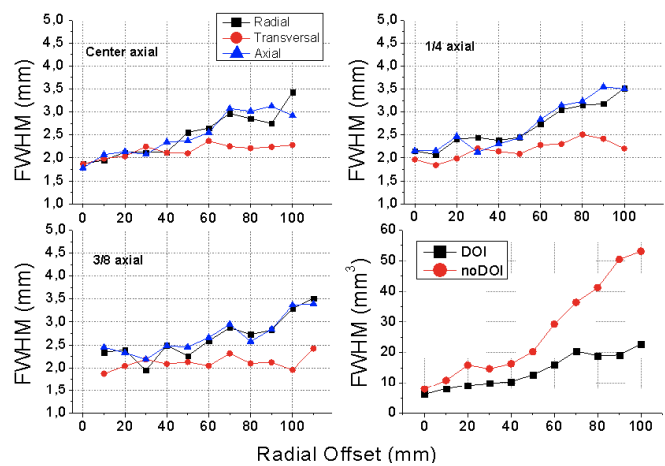


Fig. 9. Measured spatial resolution results (FWHM) of a point source (1 mm diameter) as a function of the radial offset and for three axial positions using the LMOS algorithm. The bottom-right panel shows the volumetric FWHM comparison for data with and without photon DOI correction.

TABLE II
SPATIAL RESOLUTION FBP, FWHM (MM)

Position	Voxel 1 mm	Voxel 0.5 mm	Voxel 0.25 mm
<i>10 mm off-radial</i>			
Transverse radial	3.4	2.5	2.1
Transverse tangent.	3.0	1.8	1.5
Axial	2.5	2.1	2.2
<i>100 mm off-radial</i>			
Transverse radial	3.5	3.0	2.3
Transverse tangent.	4.9	3.9	2.7
Axial	4.0	3.9	3.1

good uniformity across the FOV, especially for the 120 mm in diameter center, as it was expected, due to the accurate DOI correction. We have calculated the volumetric FWHM for the case of sources placed at the axial center and compared with data obtained without DOI correction. We observed a high degradation toward the FOV edges.

In addition to iterative algorithms, and according to the NEMA protocol, sources at center of the axial system center, and at two radial offsets, have also been reconstructed using single slice rebinning and filtered backprojection with a butterworth filter. The image matrix was 240 mm \times 240 mm \times 154 mm, and different cubic voxel sizes tested. Table II summarizes the results at 10 and 100 mm off-radial center.

C. Recovery Coefficients in Warm Background

The recovery coefficients for these tests, named RC_i , are calculated in a similar way as the NU-2008 [22]. To obtain these coefficients, volume of interest (VOI) for each rod with dimensions of twice its diameter and 25 mm height are considered. The intensity of the voxels inside of each VOI is summed axially. The voxel corresponding to the highest value is selected as the x - y profile coordinate. The z -profile average is calculated and divided by the background VOI (35 mm diameter and 25 mm height). The resulting ratio is divided by

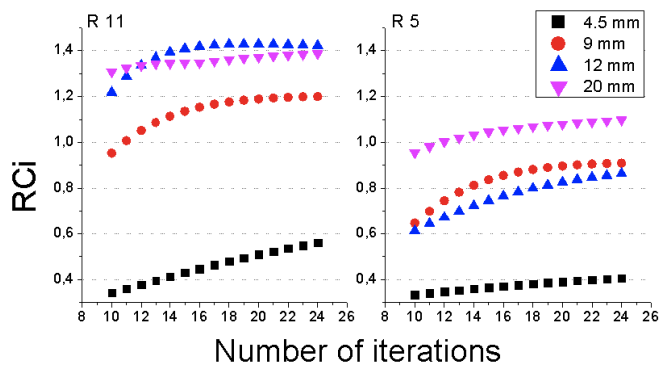


Fig. 10. RCi as a function of the number of iterations using the MLEM algorithm, for different rod diameters and for two rod/background concentrations namely 11 (left) and 5 (right).

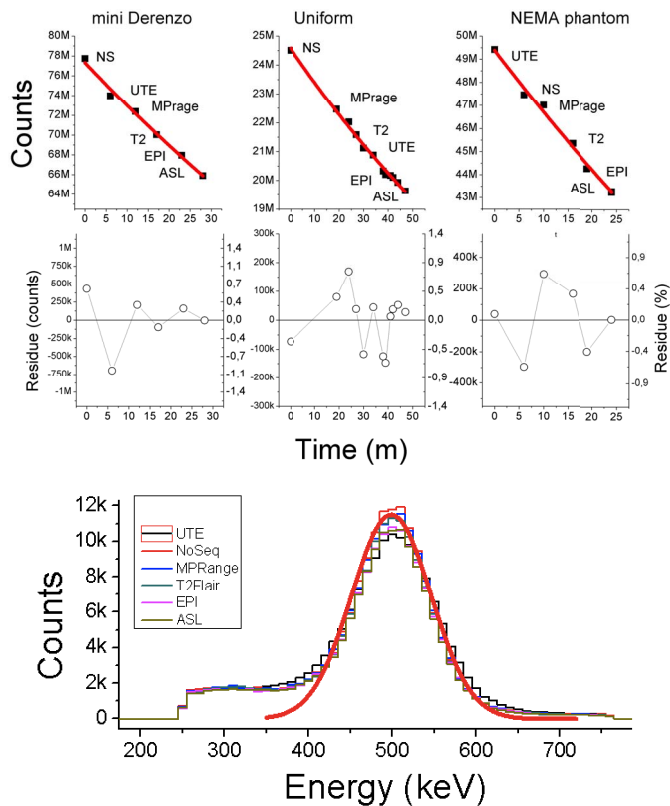


Fig. 11. System performance as a function of the MR sequence. Top panels show the number of counts as a function of time (MR sequence type) for three phantoms. Center panels depict the residue of a fit carried out with the exponential decay curve of ^{18}F . Bottom plots exhibit the energy profiles for one detector module and for the different sequences.

the known concentration ratio [21]. We have determined the RCi for two concentration ratios namely 11 and 5 ($\pm 20\%$), respectively. We calculated the RCi for inserts with diameters of 4.5, 9, 12, and 20 mm. The other two inserts were contaminated with higher activities while filling. The images were reconstructed using MLEM including attenuation corrected, but no filter was applied to those. Fig. 10 shows the determined RCi as a function of the number iterations.

D. PET Performance Versus MR Sequences

The effect of different MR sequences was evaluated with different FDG filled phantoms. We have measured the count

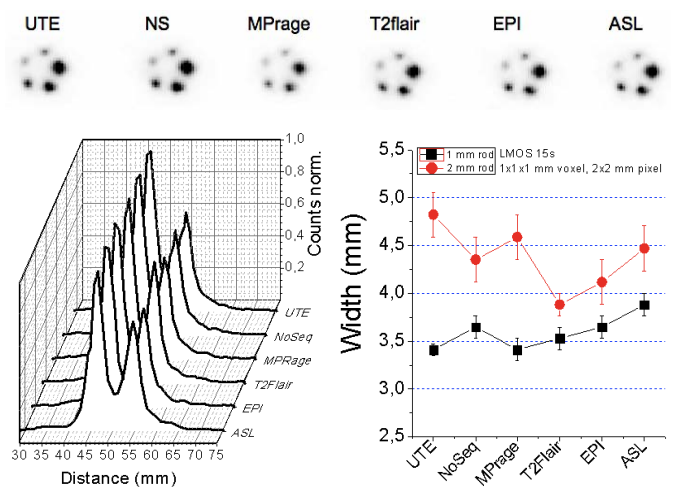


Fig. 12. Top: images acquired of the small animal NEMA phantom as a function of the MRI sequence (NS stands for nonsequence). Bottom-left: profile across the 1 and 2 mm in diameter rods. Bottom-right: measured Gaussian widths versus MRI sequence.

rates for all phantoms as a function of the different MR sequences (and time). Fig. 11 top shows the number of acquired counts (prompt) as a function of time and for different MR sequences, for three phantoms. The data points (black squares) have been fitted to an exponential decay curve fixing the ^{18}F half-life (red line in the top panels). Initial activities were 12, 40, and 32 MBq, for the named mini-Derenzo, Uniform and NEMA phantoms, respectively. We have estimated the percentage of randoms events, and they are in the range of 2%–4%. The panels below depict the residue (open circles) in absolute counts (left axis) and in percentage (right axis). No significant count losses are observed, all differences are below 1%.

In addition to count rate studies, we have also studied the energy profiles for some detectors for all sequences. We did not observe significant differences among all the measurements. As an example, Fig. 11 bottom shows the energy profile for one detector when running experiments with the NEMA phantom. A slightly 2%–3% worsening energy resolution, but not count rate losses, was observed during UTE.

We reconstructed acquisitions of the small animal NEMA phantom using LMOS with 1 mm voxel size and 2 mm virtual pixel, see top row in Fig. 12. We analyzed a profile across the smallest rods for all cases, as plotted in the bottom-left panel. We have determined the Gaussian widths and plotted them against the sequence type without observing any significant deterioration for any particular sequence. In a further step, LMOS reconstructions of acquisitions with the PET insert but using cubic voxels of 0.7 mm and virtual pixels of 1.4 mm were also possible, showing an improved image quality (FWHM) of about 10%.

The image quality phantom for small animals was also used to provide information on the SNR and recovery coefficients, as a function of the MR sequence. The data were reconstructed using OSEM (CASTOR) since it allowed varying the number of iterations and subsets finding the optimum for these tests. Indeed, best performance has been achieved for

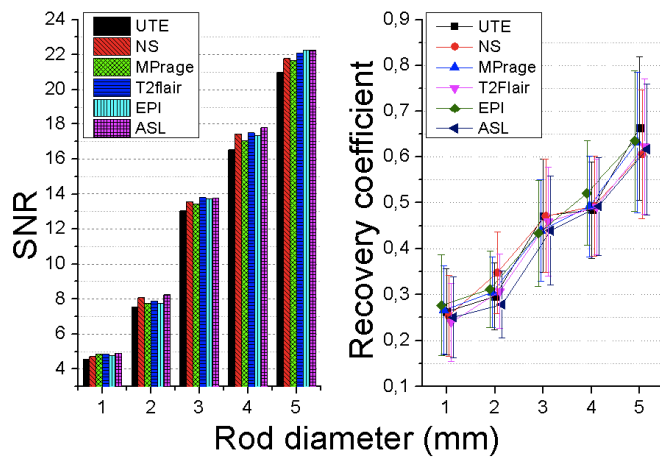


Fig. 13. SNR (left) and recovery coefficients (right) as a function of the rod diameter, and for different MR sequences, using the CASTOR algorithm.

1 or 2 iterations and 10 subsets. Moreover, the 2 mm rod was unfortunately in the exact CFOV and, using CASTOR it was possible to minimize and underestimate the mean values by computing the sensitivity matrix directly from the normalization data. The SNR was calculated as the ratio of the difference of the mean values obtained for the rods and background, to the standard deviation of the background. The VOI of the rods had diameters matching the true rod diameters and a height of 12 mm. The background was taken from a cylindrical VOI of 4 mm in diameter and 12 mm height in the center volume of the 5 rods. The RC were calculated as the maximum of the VOI over the mean value of the uniform area (25 mm diameter times 10 mm height). The standard deviation of the RC was also calculated using the methodology described in [23]. In general, both the SNR and the RC show no dependencies with the MR sequence, as shown in Fig. 13. SNR improves with the rod diameter, as expected. Also the recovery coefficients exhibit this behavior.

Additional tests to explore the effect of the MRI sequences on the PET insert performance were carried out using the mini-Derenzo phantom. The phantom was placed parallel to the patient bed. The images in Fig. 14 (top), that are in absence of an MR sequence, show the reconstructed images for data sequentially obtained with mMR PET and PET insert, left and right, respectively. The mMR PET makes use of an OSEM algorithm with voxel sizes of 1 mm \times 1 mm \times 2 mm (axial). A few rods of 2.5 mm were not well filled. The images are displayed without applying any filter. The PET insert image is obtained using MLEM with 63 iterations, whereas the mMR image is again an OSEM with 3 iterations and 21 subsets and, therefore, equivalent effective iterations. The PET insert, in contrast to the mMR image, shows the capability to resolve the 2.5 mm rods. We have plotted in Fig. 14 bottom profiles of a row of 2.5 mm capillaries for different MR sequences, without observing any degradation.

E. B1 Performance

We studied the B0 and performance of the MRI when the PET insert was placed inside and normally working.

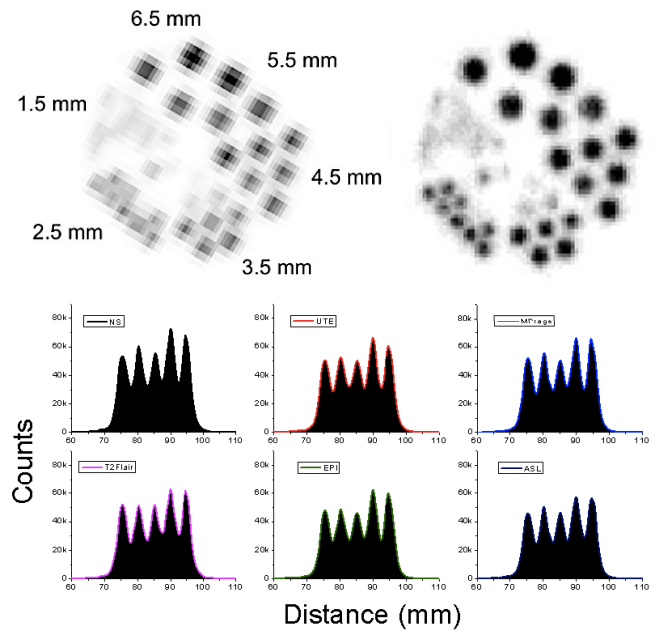


Fig. 14. Top: Derenzo phantom images acquired with the mMR PET (left) and MINDView PET insert (right), no MR sequence applied. Bottom: profiles of a row of 2.5 mm capillaries as a function of the MR sequence, obtained with the PET insert.

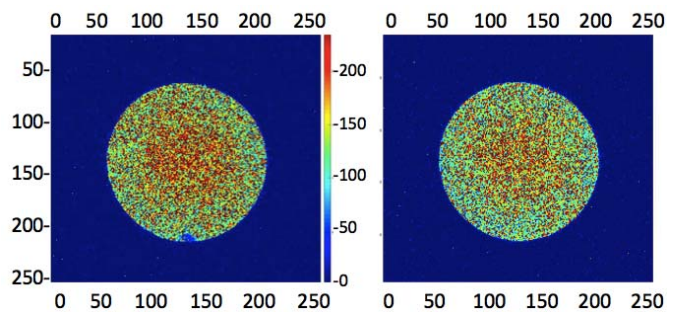


Fig. 15. SNR maps for the B1 field, without the PET insert (left) and with the PET powered ON (right). Transversal slice through the standard Siemens phantom bottle (3.75 g NiSO₄ \times 6H₂O+5 g NaCl in 1000 ml H₂O). x and y -axis are in millimeter. The SNR scale varies from 0 to 250 for both images.

A standard Siemens SNR sequence was run to retrieve information about the B1 uniformity. An SNR map was obtained for each pixel as the ratio of the mean value over the sigma of the background measurement. We did this for an acquisition without the PET (left panel in Fig. 15) and with the PET in place and powered ON (right panel). The SNR for the first case was 232, whereas this only varied to 215 with the PET inserted and powered ON (a reduction in SNR of about 7%).

F. Brain Phantom Images

Initial tests with a human brain phantom, so-called Hoffman, have been carried out in order to show the system performance with large and detail volumes. The phantom was filled with about 15 MBq of a solution of FDG and Gadolinium, and scanned for 20 min inside the mMR. The images shown in Fig. 16 are transversal views with 5 mm

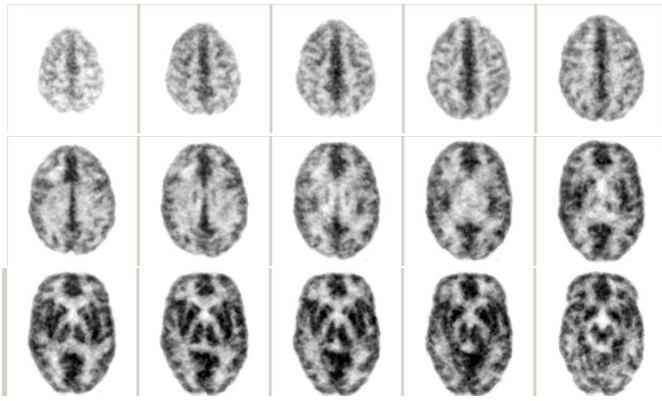


Fig. 16. Transverse views (5 mm thick) of a human brain phantom. The phantom was filled with about 15 MBq of FDG and a Gadolinium solution.

thickness. They were reconstructed using MLEM with 60 iterations. Attenuation correction on these images was based on a pilot PET image segmentation approach. A median-3-D filter with kernel size equals to 3 was used.

IV. DISCUSSION AND CONCLUSION

In this paper, we show pilot results of the brain PET insert developed under the MINDView project in terms of system performance when combined with a 3T MR. Although the PET insert has not been tested with different MR systems regarding vendors or main field strengths, we envisage a good system performance (including 7T MR) due to the followed design constrains.

The prototype design and construction have been accomplished. The system showed a physical sensitivity at the CFOV with a small size ^{22}Na source of nearing 7% for an energy range of 350–650 keV. The average energy resolution measured for all detectors and crystal volume was very similar ($\sigma = 1.5\%$) with an average value of 17.5%. This value slightly differs from expected values as shown in [13]. This might be explained because the current prototype uses photo-sensor arrays coupled to specially designed PCBs to avoid MR distortions and induced currents, and also the software collimation applied here is wider than in [13]. The detector blocks, including part of these PCBs, were inserted in temperature controlled housing keeping an average system temperature of 27.5 °C. Significant lower temperatures (10 °C–15 °C lower) might show some PET image performance improvements, however, this would cause a large and constant compressed air input flow.

Photon DOI is corrected for each LOR prior to reconstruction. This made it possible to reach spatial resolutions of 1.7 mm (FWHM), degrading at 100 mm off-radial center to only 3 mm for the radial and axial components, and 2.5 mm for the transversal. A strong image deterioration is observed when DOI is not used. Some improvements in the gamma-ray impact calibration as a function of the DOI are being currently undergoing which could improve the spatial resolution worsening dependence with the radial position.

We have shown the benefits of three iterative reconstruction algorithms. We did use LMOS for the point sources

reconstruction because 0.7 mm voxels were possible with this method. Some phantoms were also successfully reconstructed using these parameters. MLEM and OSEM (CASTOR) are well-established algorithms for PET imaging. They present benefits and drawbacks, and this is why both have been arbitrarily used. MLEM, although slow in some implementations, in the current tested, made use of 4 GPU and, therefore, reconstruction times of few minutes were feasible for the range of 20–30 iterations. On the other hand, OSEM exhibited a good image analysis of the small quality NEMA phantom.

Both RCi obtained with the custom phantom having inserts in a warm background, and the RC obtained from the small animal NEMA image quality phantom agree well with expected values. In the case of the RCi, it was complex to provide the exact true concentration ratio and, therefore, slightly values higher than 1 are obtained for the largest inserts.

The system works well under any of the tested MR sequences that are suitable for brain imaging. Several FDG fillable phantoms were scanned using the PET insert inside the 3T MR of the Siemens mMR. Count rate degradations were not observed of the insert PET data for any of these sequences, including strong EPI or UTE. Regarding the detectors performance, they did not also show any deterioration.

Concerning performance comparison with a state-of-the-art whole body PET system, the PET insert shows an improved spatial resolution as for instance observed through the mini-Derenzo. Currently, the system is in Klinikum rechts der Isar (Munich) and patients selection is undergoing.

ACKNOWLEDGMENT

The authors would like to thank all members of the MINDView consortium for their support on this project. They would also like to acknowledge the help from Bruker team. Experimental data at the UPV Bunker could not have been achieved without the help of M. Hassan from U. Valencia.

REFERENCES

- [1] T. Abraham and J. Feng, "Evolution of brain imaging instrumentation," *Seminars Nucl. Med.*, vol. 41, no. 3, pp. 202–219, 2011.
- [2] G. L. Brownell and W. H. Sweet, "Localization of brain tumors with positron emitters," *Nucleonics*, vol. 11, no. 11, pp. 40–45, 1953.
- [3] I. Rausch *et al.*, "PET/MRI for oncologic brain imaging: A comparison of standard MR-based attenuation corrections with a model-based approach for the siemens mMR PET/MR system," *J. Nucl. Med.*, vol. 58, no. 9, pp. 1519–1525, 2017.
- [4] G. Schramm *et al.*, "Validation of ZTE head attenuation correction in the GE SIGNA PET/MR-initial results," *J. Nucl. Med.*, vol. 58, no. S1, p. 644, 2017.
- [5] H. Herzog *et al.*, "High resolution BrainPET combined with simultaneous MRI," *Nuklearmedizin*, vol. 50, no. 2, pp. 74–82, 2011.
- [6] N. J. Shah *et al.*, "Advances in multimodal neuroimaging: Hybrid MR-PET and MR-PET-EEG at 3 T and 9.4 T," *J. Magn. Reson.*, vol. 229, pp. 101–115, Apr. 2013.
- [7] K. J. Hong *et al.*, "A prototype MR insertable brain PET using tileable GAPD arrays," *Med. Phys.*, vol. 40, no. 4, 2013, Art. no. 042503.
- [8] F. Nishikido *et al.*, "Feasibility of a brain-dedicated PET-MRI system using four-layer DOI detectors integrated with an RF head coil," *Nucl. Instrum. Methods Phys. Res. A Accelerators Spectrometers Detectors Assoc. Equip.*, vol. 756, pp. 6–13, Aug. 2014.
- [9] F. Nishikido *et al.*, "Development of 1.45-mm resolution four-layer DOI-PET detector for simultaneous measurement in 3T MRI," *Radiol. Phys. Technol.*, vol. 8, no. 1, pp. 111–119, 2015.

- [10] A. Del Guerra *et al.*, "TRIMAGE: A dedicated trimodality (PET/MR/EEG) imaging tool for schizophrenia," *Eur. Psychiatry*, vol. 50, pp. 7–20, Apr. 2018.
- [11] J. M. Benlloch *et al.*, "The MINDVIEW project: First results," *Eur. Psychiatry*, vol. 50, pp. 21–27, Apr. 2018.
- [12] A. J. González *et al.*, "The MINDView brain PET detector, feasibility study based on SiPM arrays," *Nucl. Instrum. Methods Phys. Res. A Accelerators Spectrometers Detectors Assoc. Equip.*, vol. 818, pp. 82–90, May 2016.
- [13] A. González-Montoro *et al.*, "Performance study of a large monolithic LYSO PET detector with accurate photon DOI using retroreflector layers," *IEEE Trans. Radiat. Plasma Med. Sci.*, vol. 1, no. 3, pp. 229–237, May 2017.
- [14] G. Delso *et al.*, "Performance measurements of the siemens mMR integrated whole-body PET/MR scanner," *J. Nucl. Med.*, vol. 52, no. 12, pp. 1914–1922, 2011.
- [15] A. J. González *et al.*, "A brain PET insert MR compatible: Final design and first results," in *Proc. IEEE Nucl. Sci. Symp. Med. Imag. Conf. Room Temperature Semicond. Detector Workshop (NSS/MIC/RTSD)*, Strasbourg, France, 2016, pp. 1–5.
- [16] L. Moliner *et al.*, "Implementation and analysis of list mode algorithm using tubes of response on a dedicated brain and breast PET," *Nucl. Instrum. Methods Phys. Res. A Accelerators Spectrometers Detectors Assoc. Equip.*, vol. 702, pp. 129–132, Feb. 2013.
- [17] A. Iborra *et al.*, "IRIS projector adaptation for PET scanners based on monolithic crystals," in *Proc. IEEE Med. Imag. Conf.*, 2017.
- [18] T. Merlin *et al.*, "CASToR: A generic data organization and processing code framework for multi-modal and multi-dimensional tomographic reconstruction," *Phys. Med. Biol.*, vol. 63, no. 18, 2018. [Online]. Available: <https://doi.org/10.1088/1361-6560/aadac1>
- [19] A. J. González *et al.*, "A PET design based on SiPM and monolithic LYSO crystals: Performance evaluation," *IEEE Trans. Nucl. Sci.*, vol. 63, no. 5, pp. 2471–2477, Oct. 2016.
- [20] A. Gonzalez-Montoro *et al.*, "A method to measure the intrinsic detector resolution on monolithic crystals," in *Proc. IEEE Med. Imag. Conf.*, 2017.
- [21] L. Moliner *et al.*, "Performance characteristics of the MAMMOCARE PET system based on NEMA standard," *J. Instrum.*, vol. 12, no. 1, 2017, Art. no. C01014.
- [22] *Performance Measurements of Small Animal Positron Emission Tomographs*, document NU 4-2008, Nat. Elect. Manuf. Assoc., Arlington, VA, USA, 2008.
- [23] Q. Bao, D. Newport, M. Chen, D. B. Stout, and A. F. Chatzioannou, "Performance evaluation of the inveon dedicated PET preclinical tomograph based on the NEMA-NU4 standards," *J. Nucl. Med.*, vol. 50, no. 3, pp. 401–408, 2009.